Microfluidic Interposers: Enabling Next-Generation Biosensing by Integrating Microfluidic Structures on PICs

Sam Robison, Ziyu Wang

June 15, 2024

Contents

1 Introduction

1.1 Motivation

Over the past few decades, novel integrated photonic devices have provided a wealth of possibilities for manipulating optical fields at the micron scale[1, 2, 3]. As fabrication techniques continue to mature, these specialized devices have gained traction in many applications, owing to their compact size, their compatibility with production-scale manufacturing techniques, and the precise optical control they enable. Different types of material platforms have been developed, such as silicon[4, 5, 6], silicon on insulator (SOI)[7, 8], gallium arsenide (GaAs)[9, 10], indium phosphide (InP)[11, 12], and lithium niobate (LN)[13, 14, 15]. Among them, thin film lithium niobate (TFLN) has piqued the interest of many research groups due to its high speed electro-optic response, low optical loss, large optical nonlinearity and large acousto-optical coupling coefficient. Using this platform, a variety of interesting phenomena have been demonstrated, including optical parametric oscillators (OPOs)[16], Kerr optical frequency combs[17], high speed electro-optical modulation[18, 19], and microwave-optical frequency converters[20].

The generation of quantum-states of light, such as squeezed vacuum depends on nonlinear optical effects. Recently, several research groups have demonstrated the generation of squeezed vacuum using TFLN platforms [21, 22, 23]. A squeezed state refers to non-classical state of light, in which the quantum noise of one measurement quadrature has been reduced (squeezed) at the expense of in increase in quantum noise in the other quadrature (anti-squeezed). This reduction in quantum noise allows high-precision measurements beyond the standard quantum limit (SQL), which have notably been demonstrated in gravitational wave detection[24, 25]. The high $\chi^{(2)}$ nonlinearity in TFLN enables squeezing by degenerate parametric down-conversion in a sub-threshold OPOs, which reduces the noise in the phase quadrature of the optical field and may enable a next-generation of quantum-enhanced bio-sensors.

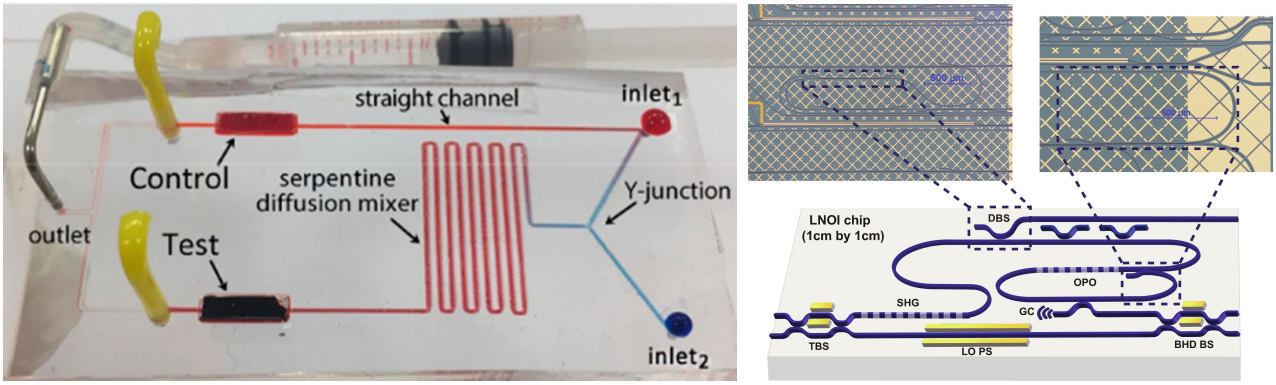

Figure 1.1: Microfluidic system and photonic chip. Left:[26]. Right:[23].

One challenge in fabricating chip-scale bio-sensors, however, is the fundamental mismatch between the length scales of microfluidic systems and TFLN photonic chips. As shown in Fig. 1.1, the size of a microfluidic system is on the order of centimeters, owing to the necessary tubing, while the size of a photonic chip is on the order of millimeters.

To address this issue, we developed a robust fabrication process for integrating a microfluidic systems with our quantum photonic chips. Fig. 1.2 shows a cross-section of the three-layer microfluidic interposer stack that we proposed. The light blue sections indicate the microfluidic system, which is comprised of polydimethylsiloxane (PDMS), while the dark blue section indicate the via and channels through which our samples will flow. The green section shows the photonic chip.

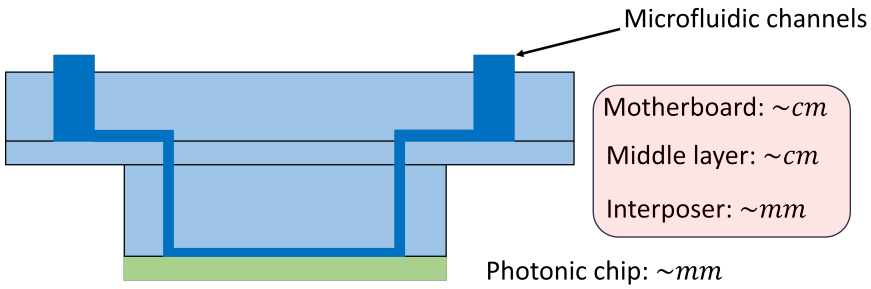

Figure 1.2: Diagram of the side view of the microfluidic system integrated with photonic chip.

1.2 Benefits to the SNF Community

As integrated photonic platforms continue to mature, new possibilities in bio-sensing will emerge and usher in exciting new discoveries. Integrating microfluidic systems with these photonic platforms will be an important aspect of the bio-sensing toolbox, so we wish to lay the groundwork for future advancements in the field at Stanford. We have compiled many tricks and tips that are present within the institutional knowledge at SNF into one concise report and a series of standard operating procedures (SOPs) that we hope may act as a guide for future researchers.

1.3 Project Goals

Our research group's ultimate goal is to fully integrate microfluidic test structures atop our quantum photonic devices. Given the time constraints, we divided our goals for this quarter into two main goals and a series of reach goals that would propel us towards our ultimate goal of creating quantum-enhanced biosensors:

- Main Goals
  - Optimize the soft lithography process for generating SU-8 molds
  - Fabricate an interposer layer
- Reach Goals
  - Develop the bonding techniques to create the full, three-layer stack and bond it to a silicon chip
  - Integrate an interposer atop a real photonic chip
  - Integrate multiple interposers on a single motherboard chip

2 Fabrication Process Development

In this section, we provide a detailed description of our fabrication process for constructing microfluidic interposers and integrating them with photonic devices. We first introduce the philosophy of our project's road map then outline the specific processes and fabrication recipes we used in each step of the process flow. Finally, we describe the design of experiments (DoE) and metrics of success we used to optimize each step in the process.

2.1 Project Road Map

The fabrication process for constructing a microfluidics interposer may be divided into three main tasks:

- Making SU-8 molds (Sec. 2.3.1)
- Curing PDMS (Sec. 2.3.2)
- Bonding PDMS to silica and PDMS (Sec. 2.3.3)

We adopted a serial process development philosophy, which is outlined in 2.1, to test, evaluate, and optimize each of these tasks individually. Where applicable, we developed a design of experiments to explore the parameter space of each process step and find the optimal recipe before moving on to the subsequent process steps.

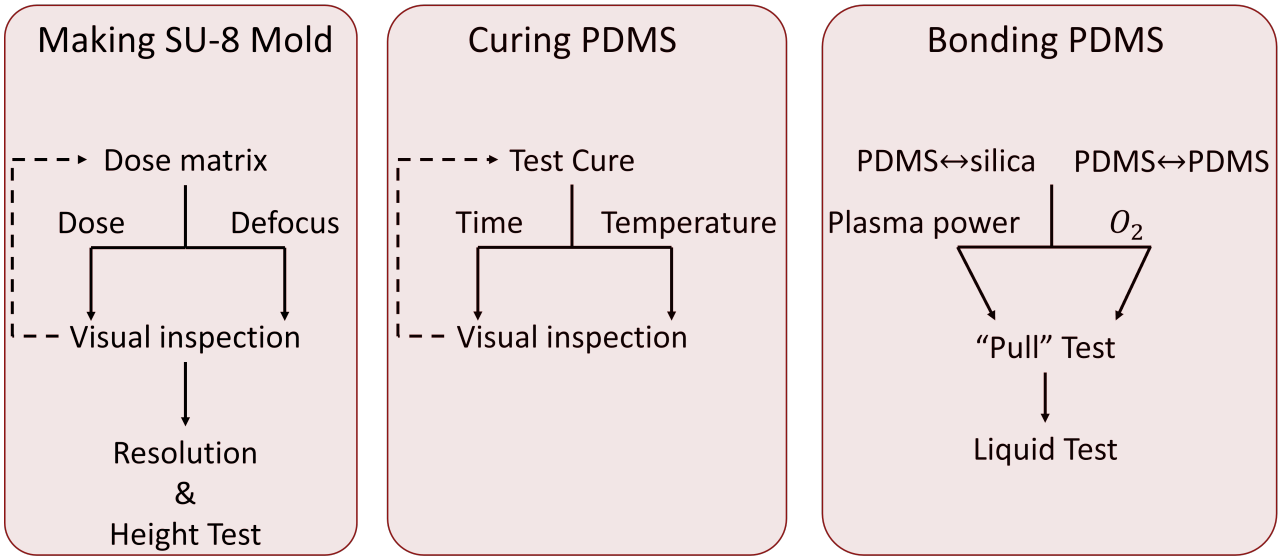

Figure 2.1: Project Road Map.

2.2 Device Design

In this subsection, we describe our designs for the overall microfluidics stack, as well as the channel designs and the test structures that we implemented.

2.2.1 Microfluidics Stack

Our design for a microfluidic interposer featured a stack of three layers: a) the motherboard, b) a thin-membrane middle layer, and c) the interposer. The motherboard provides an interface between the interposer and the necessary tubing required to flow liquid through the device. The middle layer closes the channels on the motherboard layer and provides a via down to the interposer. Finally, the interposer forms the channels that interface with the photonic chip and deliver the sample to our optical waveguide devices. The designs for each layer are shown in Fig. 2.2. The colored circles indicate where we punched holes with a biopsy punch to form vias.

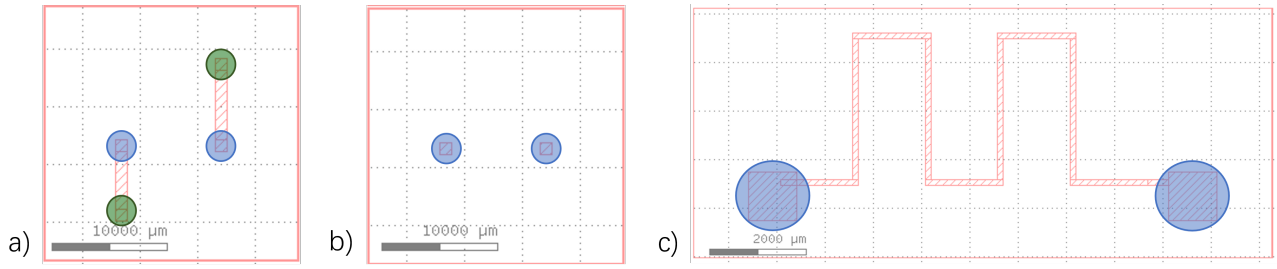

Figure 2.2: CAD design of the three layer in the microfluidic stack.

2.2.2 SU-8 Mold and Test Structures

We designed our SU-8 molds using a MATLAB repository from our lab's database to create the necessary GDS files. We aimed for a channel aspect ratio of 4:1, designing 120um wide channels with a target height of 30um. For our initial design, we included straight channels, serpentine channels, and Y channels with varying lengths and widths, as shown in Fig. 2.3.

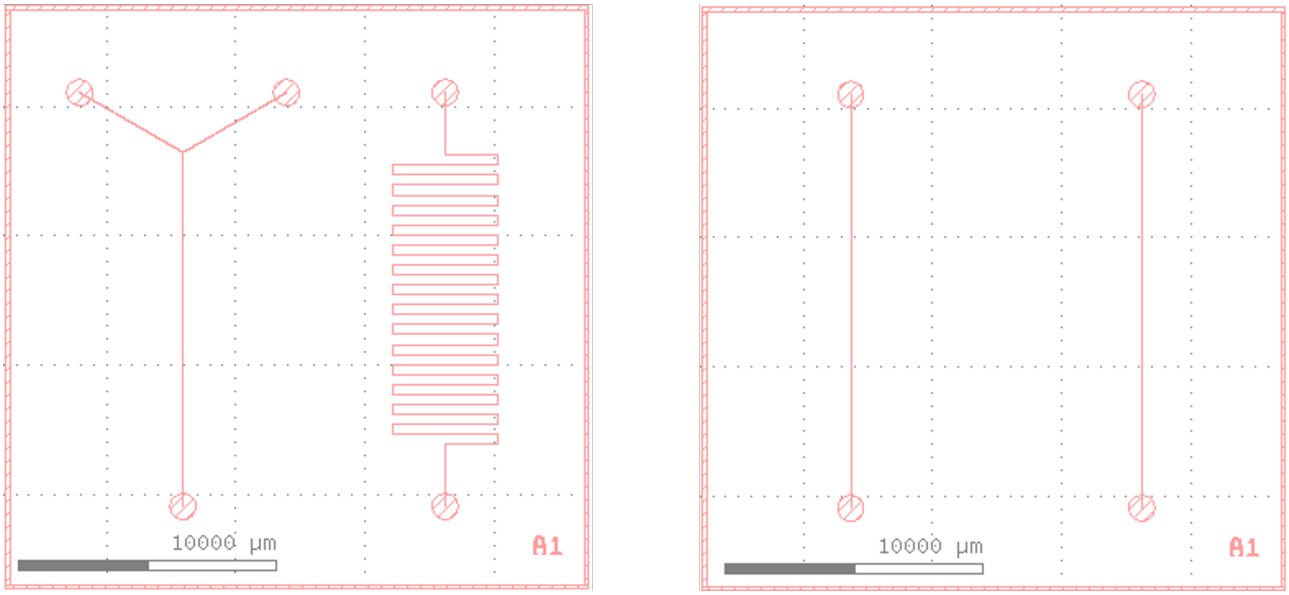

Figure 2.3: CAD designs of the initial interposer tests.

We also included two test structures on our wafer scale designs to both investigate the limits on the attainable aspect ratios and the height of our SU-8 molds. The former structures featured a series of channels of varying width to explore the lower and upper limits of channel thicknesses. The latter structures were simply large squares to provide an easy landing location to perform profilometry height measurements. The two structures are shown in Fig. 2.4.

2.2.3 Photonic Chip and Alignment Tests

We also designed a series of microfluidic structures that we aimed to integrate atop a real photonic chip containing a series of resonators spaced at a pitch of 500um, as shown in Fig. 2.5. The chip's outer dimensions were 5x12mm, which is consistent with the size scale of the actual biosensors we intend to fabricate. We designed four channel architectures to test our alignmentment capabilities. The designs show in Fig. 2.5a and Fig. 2.5b are very sensitive to displacements and require an alignment tolerance less than +/- 60um, while the designs in Fig. 2.5c and Fig. 2.5d are alignment agnostic.

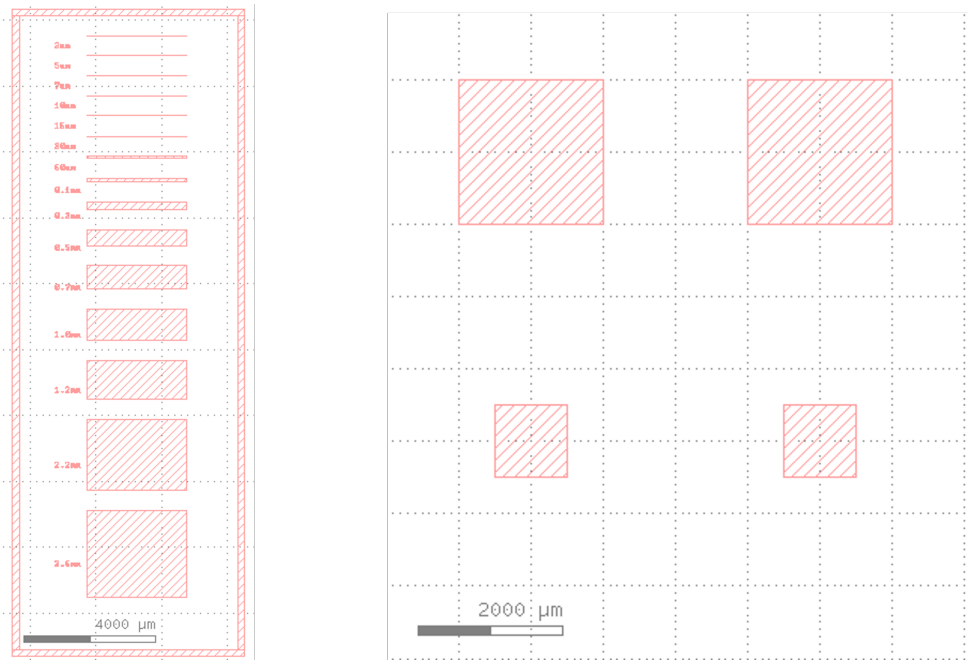

Figure 2.4: CAD design of the SU-8 test structures.

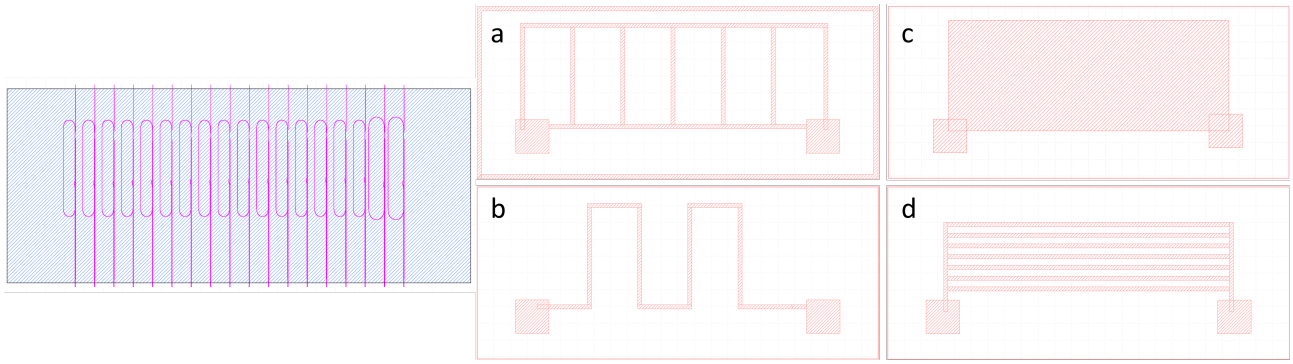

Figure 2.5: CAD file of photonic chip and four designs of microfluidic channels.

2.3 Fabrication Process Flow

In this subsection, we provide a detailed description of each step in the fabrication process. The process used to evaluate the efficacy and optimized each step is detailed in a later section.

2.3.1 Making the SU-8 Mold

We first constructed a mold for the microfluidic structures using soft lithography techniques, as shown in Fig. 2.6. SU-8 is a commonly used photoresist for this task, as it is mechanically durable, adheres to a variety of materials, and may be spun into thick films at high aspect ratios. [27] [28] We fabricated our molds atop k-test silicon, both in full wafers and as pre-diced chips.

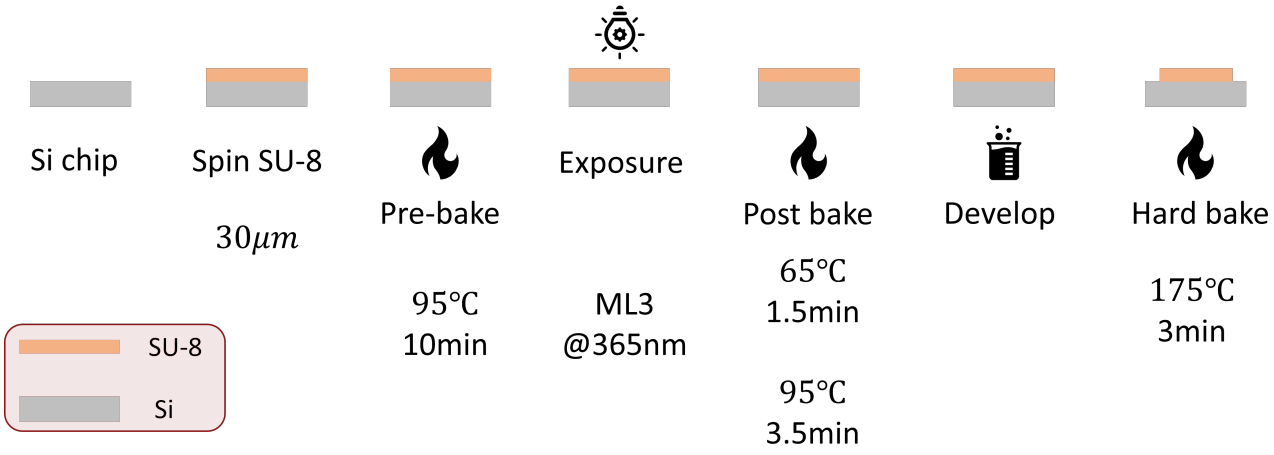

Figure 2.6: Diagram of the process of making SU-8 mold.

When using new k-test silicon wafers, we began the SU-8 exposure process by cleaning our silicon substrates with a 30 second rinse in acetone followed by a 30 second rinse with isopropyl alcohol (IPA). For molds constructed on diced silicon chips, we began with a 5 minute sonication in acetone followed by a 5 minute sonication in IPA to remove the protective layer of photoresist used in the dicing process. In both cases, we followed the cleaning process with a 5 minute dehydration bake at 150C.

We next spun SU-8 on the cleaned silicon substrates. SU-8 photoresist may be purchased in a variety of formulations of different viscosities, which are used to attain different film thickness. We used two such formulations, SU-8 2025 and SU-8 3025, which are two subsequent generations of SU-8 that formulated for the same nominal thickness of 25um. We initially believed the SU-8 3025 would be a superior resist, as it is a later generation; however, we found that it did not form an even film across the entire substrate when spun on pre-diced chips, while the SU-8 2025 could be spun on these chips with no issues. We used the SU-8 3025 when working with full-sized but still noticed streaking in the resist across the wafer due to particulates in the bottle.

The thickness of the resulting SU-8 film after spinning is a function of the spin velocity, which the manufacturer of SU-8, Kayaku, has characterized in a series of spin curves, shown in Fig. 2.7.

We targeted a thickness of 30um, so we chose a velocity of 2500rpm, and our spin recipe was as follows:

1. Spin at 500 rpm for 10 seconds with a 100 rpm/s ramp rate.
2. Spin at 2500 rpm for 30 seconds with a 300 rpm/s ramp rate.

3. Decelerate to 0 rpm with a ramp rate of 1000 rpm/s.

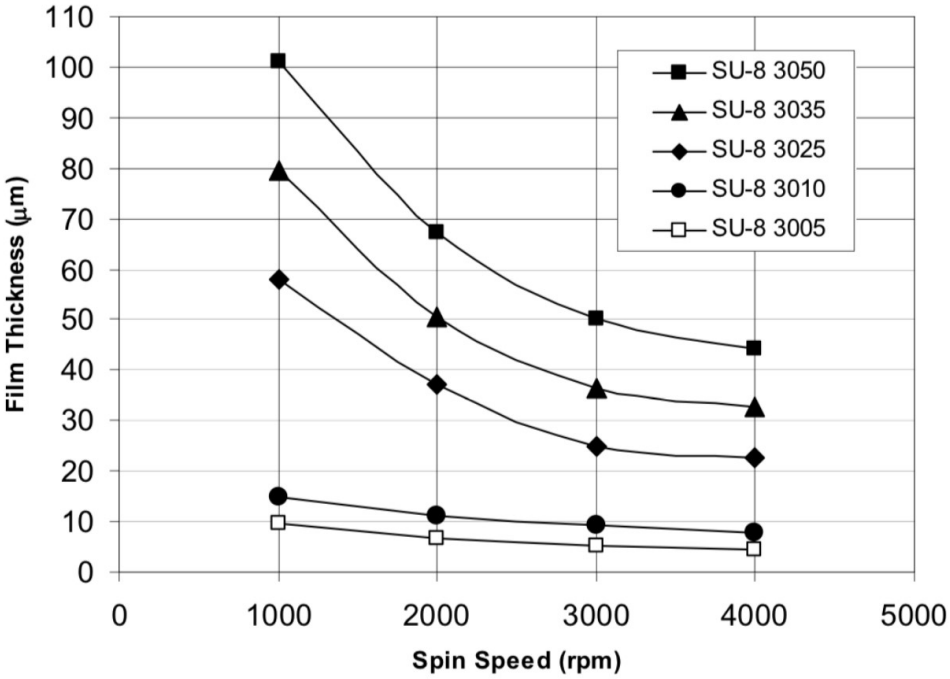

Figure 2.7: Spin curves for SU-8 3000.

After spinning the SU-8, we cleaned any stray SU-8 from the backside of the substrate then performed a 10 minute pre-bake at 95C to bake off any excess solvent. We then exposed our design patterns using the ML3, which is maskless photolithography tool with an optimal exposure wavelength of 365nm. It should be noted that SU-8 is a negative photoresist, so the areas that are intended to remain as the mold should be exposed.

We then performed a two step post-exposure bake featuring a 1 minute bake at 65C followed by a 3 minute back at 95C. We used SU-8 Developer to develop the molds and agitated them manually during the development process to remove the unexposed resist. The development time varied between the different SU-8 formulations, as well as between different bottles of SU8 developer depending on their age. The final step in the SU-8 mold fabrication process was a hard-bake for 3 minutes at 175C, which removed cracks in the SU-8 and greatly improved the quality of the structures.

In addition to creating molds using soft lithography techniques, we experimented with resin printed molds but found that the surface roughness from the printing process resulted in PDMS structures of insufficient quality. It should be noted, however, that resin printing PDMS molds is a standard practice and may result in high quality PDMS structures if the printing orientation is optimized. We simply chose not to explore this option further due to time constraints.

2.3.2 Curing PDMS

Curing PDMS is a relatively straightforward task but features several key steps to ensure a high-quality final product. The overall process consists of mixing a silicone base with a cross-linking agent and baking the PDMS until it is cured, although it will cure at room temperature after about 24 hours.

The standard mixture ratio is 10:1 base to cross-linker. We weighed out the two components on a digital scale then placed the mixture into the Thinky Mixer for a 2 minute spin cycle and

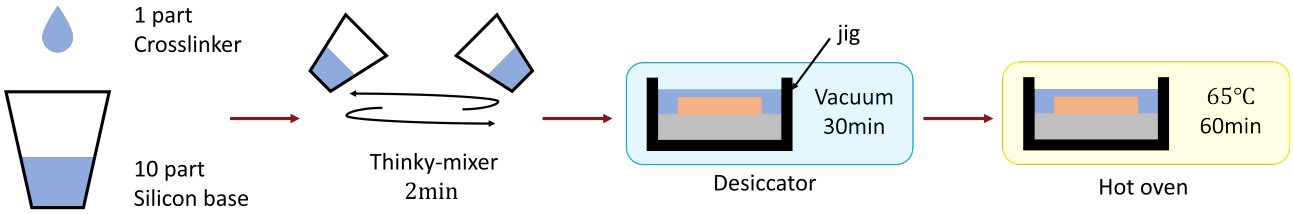

Figure 2.8: Diagram of the process of curing PDMS.

2 minute degassing step. The mixing process inherently causes air bubbles to form in the PDMS, so the mixture should be placed in a vacuum desiccator for 30 minutes to remove the bubbles. However, the process of pouring the PDMS into the mold also generates bubbles, so the desiccation step should be performed after the PDMS has been poured.

When creating thick PDMS structures, it is necessary to encase the SU-8 mold in a jig with rigid sidewalls to prevent the PDMS from spilling over the edges of the mold. The material of the jig should be compatible with the desired curing temperature. We 3D printed jigs in PLA plastic and limited our curing temperatures to 85C, which resulted in a slightly longer cure time compared to a higher temperature bake. Even with a reduced temperature, our 3D printed molds shrank in the oven and permanently encased the SU-8 molds. Alternatively, thin PDMS structures may be formed by spin coating the PDMS atop the SU-8 mold.

The time required to cure our PDMS structures varied widely depending on the thickness and surface area of the desired geometry; however, baking for an hour at 85C was typically sufficient. We considered the PDMS to be fully cured when it was no longer tacky when touched. Generally speaking, there is no downside to over-curing the PDMS, so one may safely air on the side of longer cure times.

2.3.3 Bonding PDMS

The final step in our fabrication process is to construct the full device stack, which may be divided into two individual processes: a) bonding PDMS to the silicon dioxide cladding of the photonic chip and b) bonding the PDMS layers to the one another.

2.3.3.1 PDMS to SiO2 Bonding

The functionality of microfluidic structures relies on creating water-tight bonds at the interfaces of the channels and the substrate, so it was crucial that we be able to consistently bond PDMS to silicon dioxide. PDMS will readily bond with other silicon-based materials provided that its surface is activated, which is typically achieved using corona discharge or an oxygen surface treatment.[29] We opted for the latter, given the infrastructure available in SNF.

By exposing PDMS to an oxygen-rich plasma, methyl groups on the surface may be replaced with silanol groups, which can form bonds with the another activated surface. [29] In order to reduce the complexity and cost of our fabrication tests, we opted to bond PDMS to the native oxide on k-test silicon rather than using oxide deposited with high density plasma enhanced chemical vapor deposition, as our future photonics devices will contain [23].

We performed our initial tests using the Asher in the flexible cleanroom and found that we were unable to form an instantaneous bond with the typical parameters used by other groups working with PDMS. We began working with the PE-50 in SNF, as the community has a standard recipe for bonding PDMS with the PE-50. We initially found the same results that our activated PDMS would not form a bond when placed on a second piece of activated silicon.

However, we noticed that the PDMS would occasionally stick to the original piece of silicon that we used as a carrier chip in the plasma etcher. We hypothesized that this errant bonding

was due to small gaps between the PDMS and the silicon, which allowed oxygen plasma to flow between the two materials. Though the reasons are not clear to us, it appeared that the close proximity between the two pieces while in the plasma etcher caused them bond more readily. Using this observation, we performed a DoE to determine the correct plasma parameters and developed a method that we dubbed instantaneous bonding by which we suspended a piece of PDMS above the silicon chip using two smaller pieces of PDMS, plasma treated the stack, then applied pressure to the top of the PDMS to bond it to the surface. This method resulted in a strong, permanent bond after only one minute of pressure. It should be noted that both the PDMS and silicon chips were cleaned using magic tape before the bonding process.

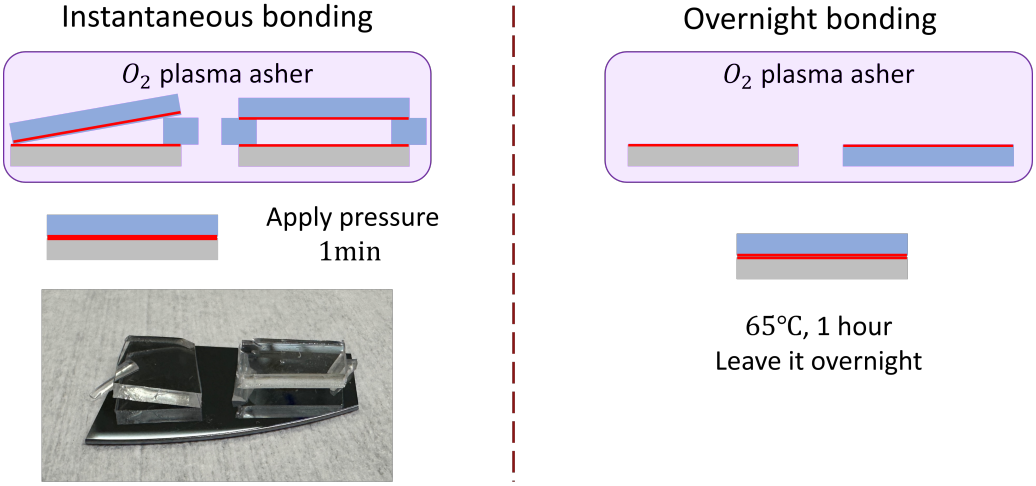

Figure 2.9: Diagram of the process of bonding PDMS to silica/PDMS.

Interestingly, when we re-examined some of our initial bonding tests, we found that some of the pieces we thought were un-bonded had actually formed a tight bond in the interim time. After consulting with SNF staff, we were informed that the plasma bonding process may be enhanced by baking the two pieces after performing the plasma treatment. With this information, we performed another DoE to develop a method we termed overnight bonding, in which the PDMS and silicon are both laid flat during the plasma treatment, the PDMS is flipped onto the silicon, the two are baked for 1 hour at 65C, and the stack is left overnight. This method similarly resulted in a tight, permanent bond. It is important that the initial contact of the PDMS and silicon be in the correct orientation because we found that the bond will not form correctly if the PDMS is readjusted from its original position.

2.3.3.2 PDMS to PDMS Bonding

In addition to bonding the PDMS interposer to our photonic chip, we also required the capability to bond the three pieces of PDMS in our microfluidics stack to one another. While plasma bonding would is a suitable method for bonding two pieces of PDMS, it must be completed quickly, as the surface only remains activated for a matter of a couple minutes. On the other hand, a common technique known as off-ratio bonding allows approximately a 40 minute window, which would provide greater flexibility in the process of aligning the different layers.

The off-ratio bonding technique, shown in Fig. 2.10, involves placing two partially cured pieces of PDMS composed of two different ratios of cross-linker solution in contact and curing them together. One piece is comprised of a 5:1 mixture (and thus has an excess of cross-linker), while the other is made up of a 20:1 mixture (and thus has a deficit of cross-linker). When the two pieces are subsequently cured while in contact, the cross-linker diffuses from the 5:1 piece into the 20:1 piece and forms a tight bond in the process.

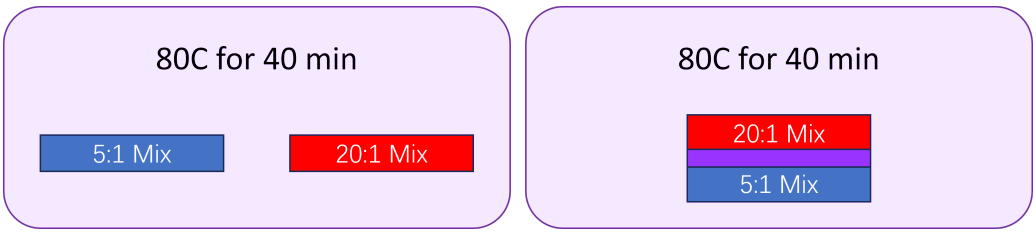

Figure 2.10: Diagram of the Process of Off-Ratio Bonding

We used the RTV-615 formulation of PDMS for our initial off-ratio bonding tests, as we were told that it is more compatible with off-ratio bonding that Sylgard-184. In our three-layer stack, we used a 5:1 mixture for the motherboard and interposer chips, while using the 20:1 mixture for the thin membrane in between. This choice was made to maximize the total amount of cross-linker in the stack to ensure a tight bond. We performed the partial cure in the same manner described in Sec. 2.3.2 except we ended the cure when the PDMS was still tacky but would no longer leave an imprint when touched with a clean room swab. Typically, the PDMS would reach this point after 30 minutes at 85C. It should be noted that the 5:1 mixture will cure more quickly than expected due to the excess cross-linker, while the 20:1 mixture will cure more slowly.

Even after a partial cure, the 20:1 mixture was not firm enough to remove from its mold without tearing the PDMS. Our solution to this problem was to align and place the motherboard atop the membrane, cure them together for 5 minutes at 85C to form a weak bond, cut the membrane around the motherboard, and remove the two bonded pieces from the thin membrane's mold. The interposer chip could then be placed on the other side of the thin-membrane and the entire stack could be baked until fully cured and bonded. This process proved very successful with the RTV-615, and we constructed a mock-up stack that is shown in Fig. 2.11.

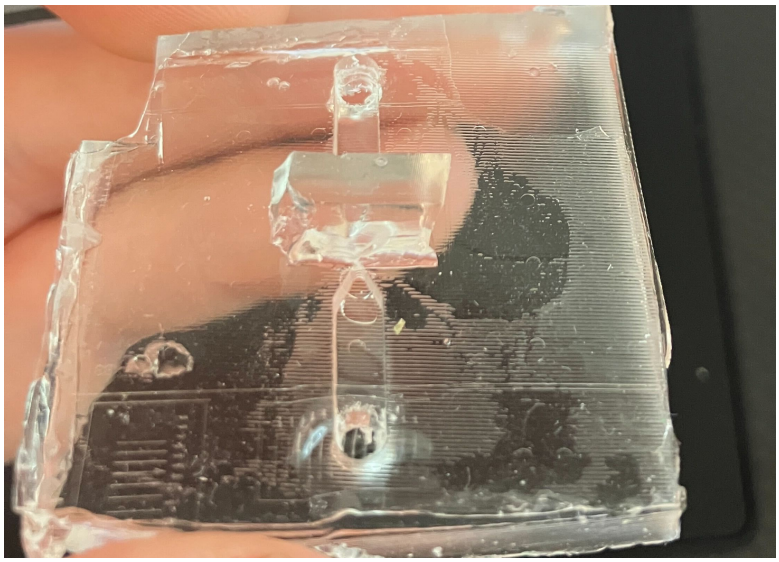

Figure 2.11: Off-Ratio Bonding Test Device

Unfortunately, we exhausted our bottle of RTV-615 cross-linker and were forced to switch to Sylgard-184 due to time constraints. We tried several DoE runs to deduce the proper partial cure times with the Sylgard-184, but they all proved ineffective.

Consequently, we opted to use plasma bonding to bond the PDMS layers to one another for the remainder of the course. The bonding technique was identical to that of the instantaneous PDMS to silicon bonding described in the previous subsection. Luckily, our alignment constraints were not too stringent between layers, so we were able to successfully build a full

microfluidic stack.

2.4 Design of Experiments

In this subsection, we describe the design of experiments we used to optimize both our exposure parameters when creating our SU-8 molds and our plasma parameters when performing PDMS bonding.

2.4.1 SU-8 Dose Matrix

The ML3 maskless photolithography tool has two main parameters that must be optimized when exposing an SU-8 mold: a) dose and b) defocus. The dose refers to the amount of energy that is delivered to a given area in the exposed region of the mask and is measured in $mJcm^{-2}$. If the dose level is too low, there will not be sufficient bonding in the SU-8 or adhesion to the substrate, and the SU-8 mold will be warped or washed away during the development stage. If the dose level is too high, the features will be larger and have less contrast than desired. Our application did not require high precision, so we were not sensitive to over-exposing our SU-8. The defocus refers to an adjustment in the nominal focal plane that is determined when auto-focusing the ML3's camera on the surface of the PDMS. Adjusting the defocus may be useful when using thick films of SU-8, as it may be advantageous to center the exposure in the middle of the SU-8 film.

We created a dose/defocus matrix, shown in Fig. 2.12, of small test structures across a chip to sweep these two parameters and developed each chip for different duration to determine the best combination of exposure and development parameters.

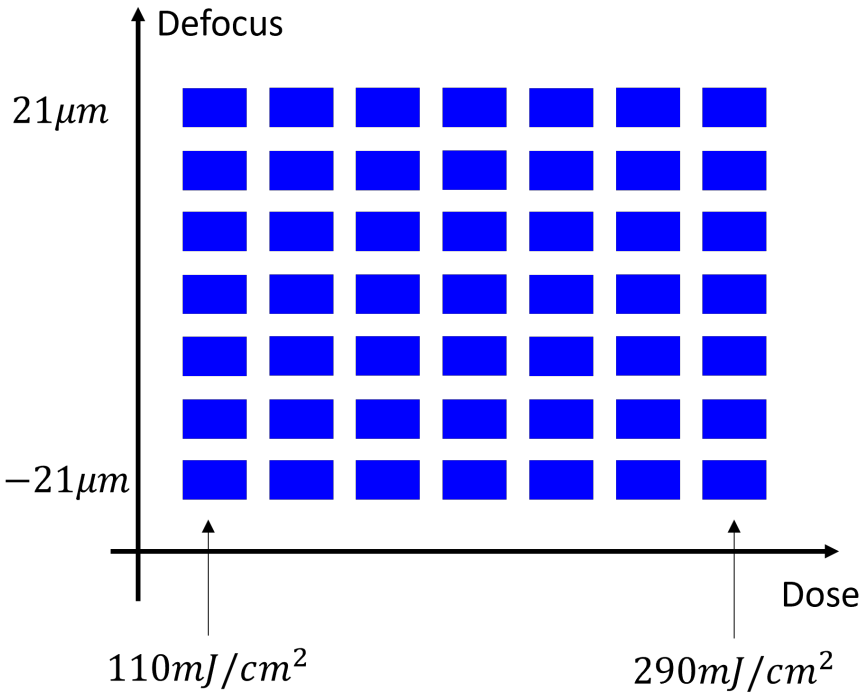

Figure 2.12: Dose matrix schematic.

Our test structures, shown in Fig. 2.13, consisted of long, wide channels and checkerboard patterns.

The long channels revealed if we were having any adhesion issues, as they would be washed away if the adhesion was not sufficient. The corners of the checkerboards, on the other hand,

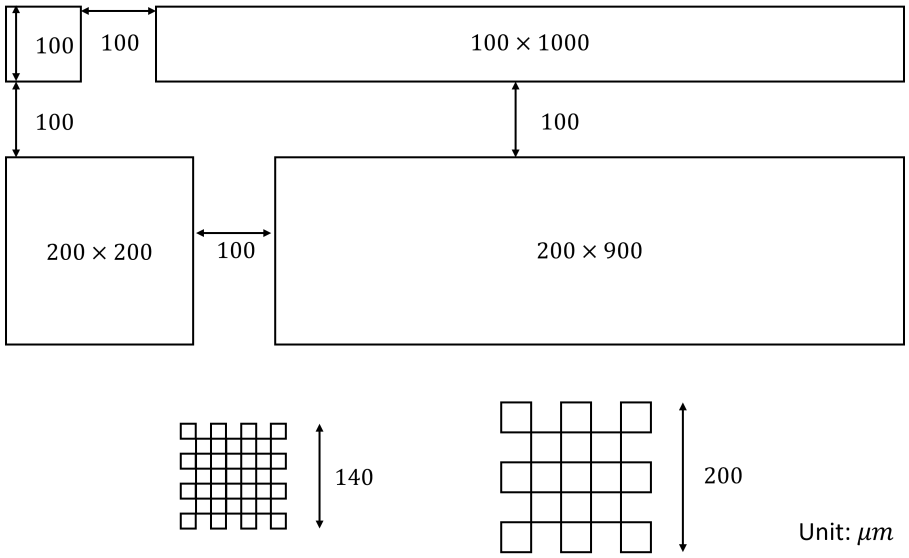

Figure 2.13: Test structures for SU-8 dose matrix.

provided an indication of whether or not the SU-8 was over/under-exposed or over/under-developed. If the corners were merged together, that suggested that the SU-8 was either overexposed or underdeveloped, while the presence of spaces or thin, wispy corners suggested the SU-8 was either under exposed or overdeveloped. We decoupled these two possibilities by comparing the results of the each dose across several development times.

2.4.2 PDMS Bonding

The PE-50 plasma etcher features also features two main parameters when performing an oxygen plasma surface activation: a) power and b) oxygen flow rate. We performed a sweep of both of these parameters when developing the instantaneous plasma bonding technique and tested the bond quality by pulling on the piece of PDMS with tweezers. When developing the overnight bonding technique, we simply swept the oxygen flow rate.

3 Results

3.1 Results of DoEs

3.1.1 SU-8 Dose Matrix

The dose/defocus matrix tests revealed a few trends that allowed us to optimize the exposure parameters. Samples with too low a dose resulted in very warped structures that were often washed away during the development step, as shown in Fig. 3.1a. Furthermore, we observed that the threshold dose for achieving good adhesion was higher for large, negative defocus values (meaning the focus was shifted below the nominal focal plane). After making this observation, we focused the ML3 camera on a bare silicon chip and found that it returned the same height as that of the SU-8 and silicon combo. This result suggests that the ML3 naturally focused on the top of the silicon chip, so large, negative defocus exposures were far out of focus at the plane of the SU-8. We performed a subsequent dose/defocus matrix with solely positive defocus values and determined +7um to be the optimal defocus.

We also noticed a trend in the resolution of the checkerboards. Smaller doses tended to cause the corners of the checkerboard to be thin and wispy, as shown in Fig. 3.1b, while larger

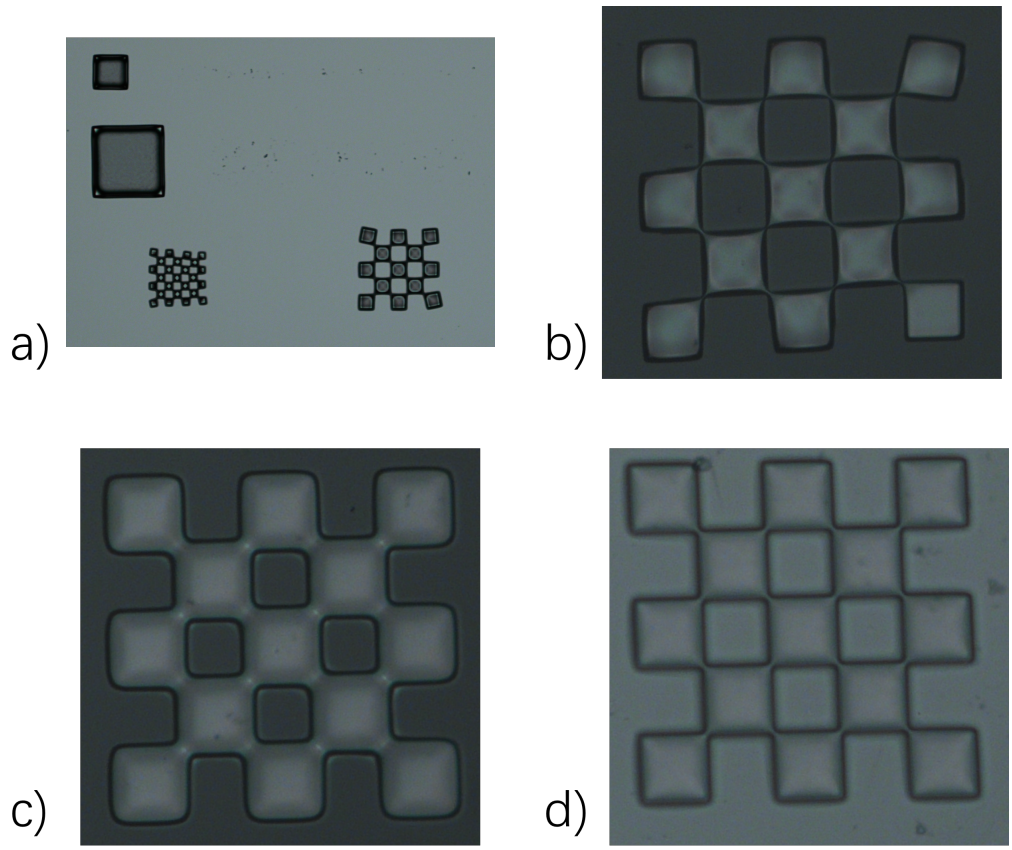

Figure 3.1: Microscope images of dose matrix test structures at different dose levels.

doses caused them to merge together, seen in Fig. 3.1c. Fig. 3.1d shows a properly exposed test structure. We arrived at an optimal dose of 350 $mJcm^{-2}$.

3.1.2 Plasma Bonding

We swept the plasma power across values of 9W, 12W, and 15W and the oxygen flow rate across values of 10ccm, 15ccm, and 20ccm to test their effects on our instantaneous bonding technique. We found that this process formed tight bonds irrespective of the parameters we selected within these ranges, which demonstrates the robustness of this methodology.

For the overnight bonding, on the other hand, we only swept the the oxygen flow rate across values of 10ccm, 15ccm, and 20ccm, while holding the power constant at 15W. We found that all three values were able to form a bond; however, only the 15ccm sample formed a strong, permanent bond. Both the 10ccm and 20ccm PDMS samples could be pulled from the silicon chip with moderate force. The results of our DoE are shown in 3.2, where green represents a tight bond and yellow represents a weak bond.

3.2 SU-8 Molds and Interposer Layer Fabrication

After optimizing our exposure and development parameters in our soft lithography process, we were able to successfully and consistently fabricate SU-8 molds on both wafer and chip scales, as shown in Fig. 3.3.

Utilizing the resolution test structures on our SU-8 molds, we determined that we could resolve channels in the SU-8 as thin as 5um wide. Any channels with more narrow widths were washed away during the development process. We also performed profilometry measurements on our test structures using the Dektak, shown in Fig. 3.4 and determined that our SU-8

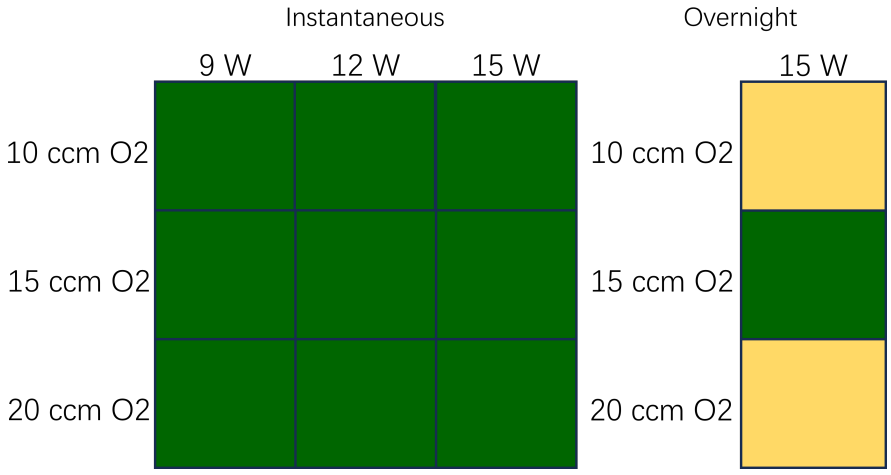

Figure 3.2: Results of PDMS Bonding DoE.

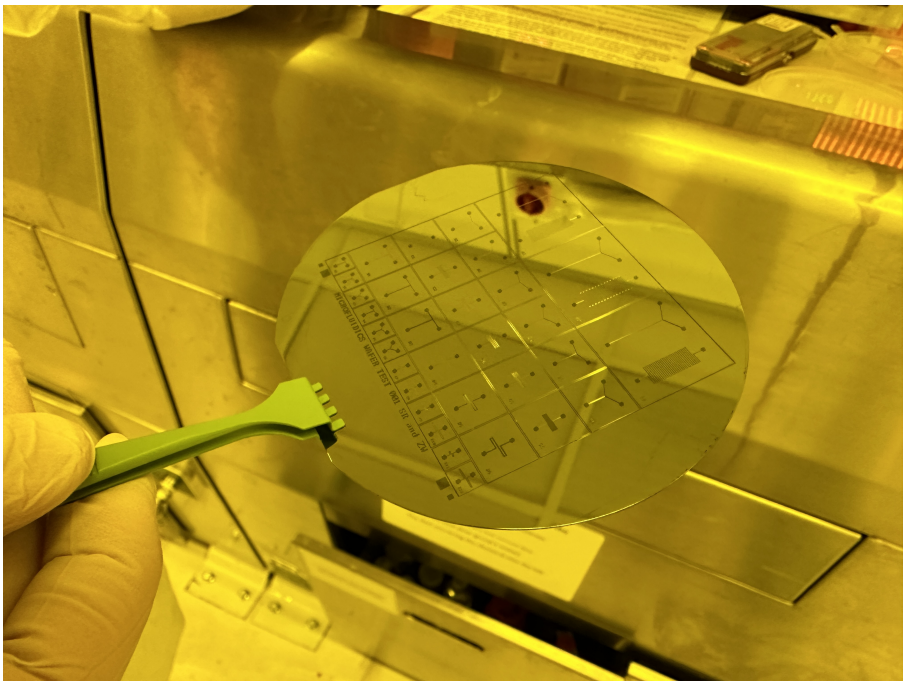

Figure 3.3: SU-8 mold on a silicon wafer.

thickness was 40um, which was higher than our target of 30um.

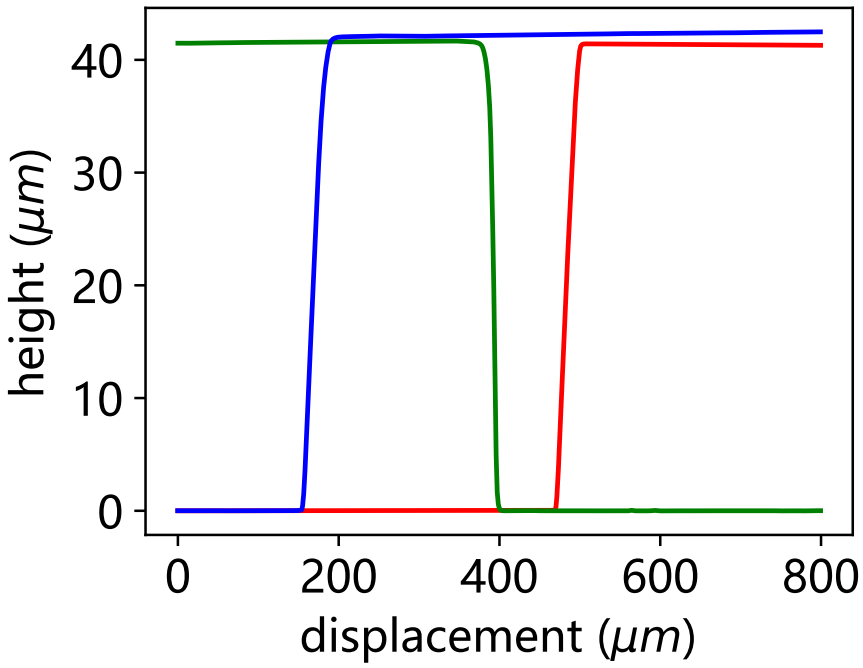

Figure 3.4: Dektak Step Height Measurements

We were also able to successfully fabricate a series of PDMS interposer layers at the wafer scale, as shown in Fig. 3.5.

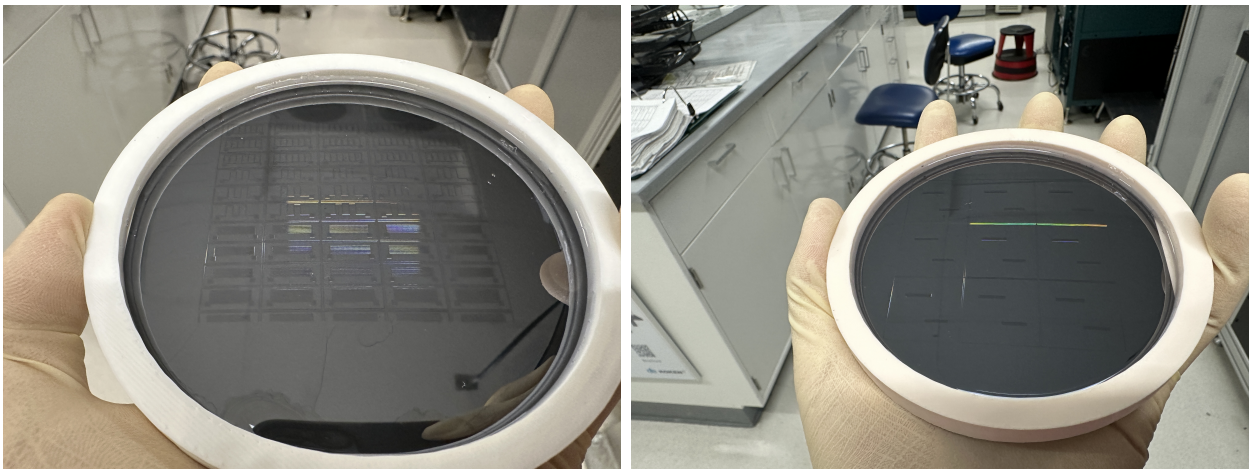

Figure 3.5: Image of channels and motherboard after curing PDMS.

We cut individual interposers from the wafer and successfully bonded them to silicon chips, as shown in Fig. 3.6 and Fig. 3.7, demonstrating that we were able to consistently achieve our main goal for this project.

3.3 Device Construction

After developing the process for fabricating and bonding individual interposer chips, we advanced to the process of constructing the full three-layer microfluidic stack, which is shown in Fig. 3.8 The two large holes were formed with a 4mm biopsy punch and formed the input ports, where 4mm OD tubing could be inserted. The input ports were connected by thin channels

Figure 3.6: Bonded Interposers

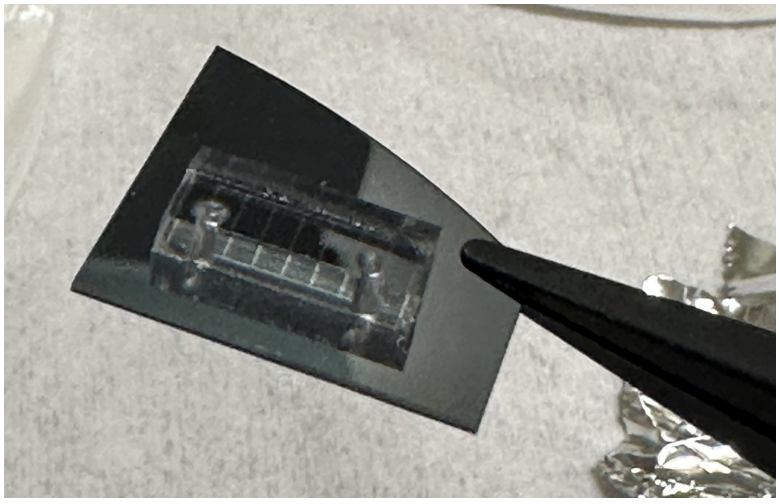

Figure 3.7: Interposer bonded to Si chip.

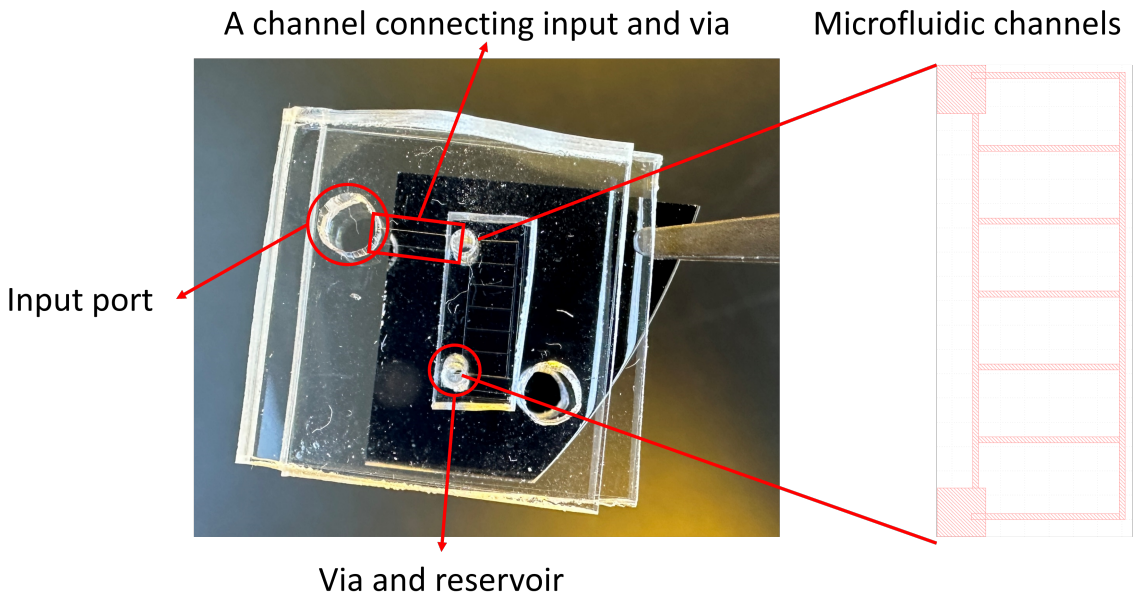

Figure 3.8: Picture of the microfluidic system bonded to Si chip.

to the vias that led down to the interposer chip. The vias were formed using a 1.5mm biopsy punch.

After bonding the full stack to a silicon chip, we performed fluid tests to ensure that the bonds were water tight and that our microfluidic structure was functional. We used a syringe to force water through the device and observed water emerging from the output pour with no extraneous leakage, as shown in Fig. 3.9. This result demonstrated that our bonds were water tight and our channels were functional.

To further investigate the performance of the device, we examined the fluid flow in situ under microscope. We concluded that our bonds were tight after observing water flowing in the intended channels, while leaving the channels formed by the chip's border free of water. The red square in Fig. 3.10 indicates the microscope's field of view during our tests.

As indicated in the design schematic, the outer border of the chip is not connected to the input port and should remain free of water while the channels are filled. Prior to injecting water into the device, both the border and channels appear as a light shade of gray indicating that they are filled with air, as shown in Fig. 3.11.

After injecting water through the input port, the channel has clearly changed to a darker shade of grey, indicating the presence of water, while the outer border remains empty. This result indicates that our bonds are water tight, even with just a $400\mu m$ gap between channels.

3.4 Alignment

We fabricated a series of mock photonic chips with SU-8 "waveguides" to provide a low-cost, low-stakes option for initial alignment tests. Unfortunately, the 40μm mock waveguides were too tall and the PDMS could not make contact with the silicon substrae below, rendering it unable to bond to the mock photonic chips. However, we learned that our alignment process must take place under a microscope given both the scale and transparency of the channels. We fabricated another mock photonic chip with 2μm thick SU-8; however, we were unable to perform further alignment tests due to time constraints. We discuss future plans in regards to alignment in Sec. 4.1.

Figure 3.9: Detecting water leakage by injecting water into the device.

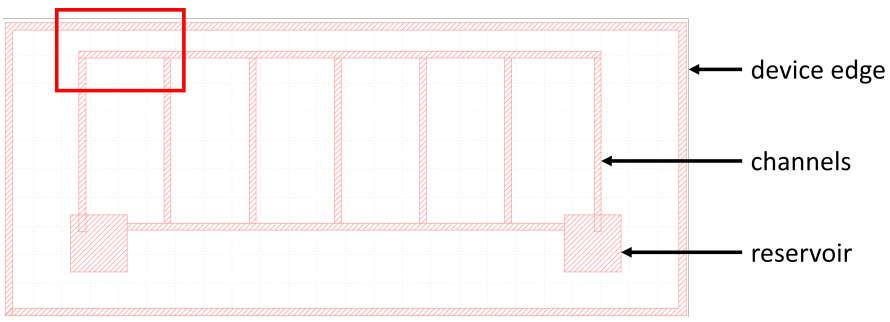

Figure 3.10: CAD design of the microfluidic channel of the real device.

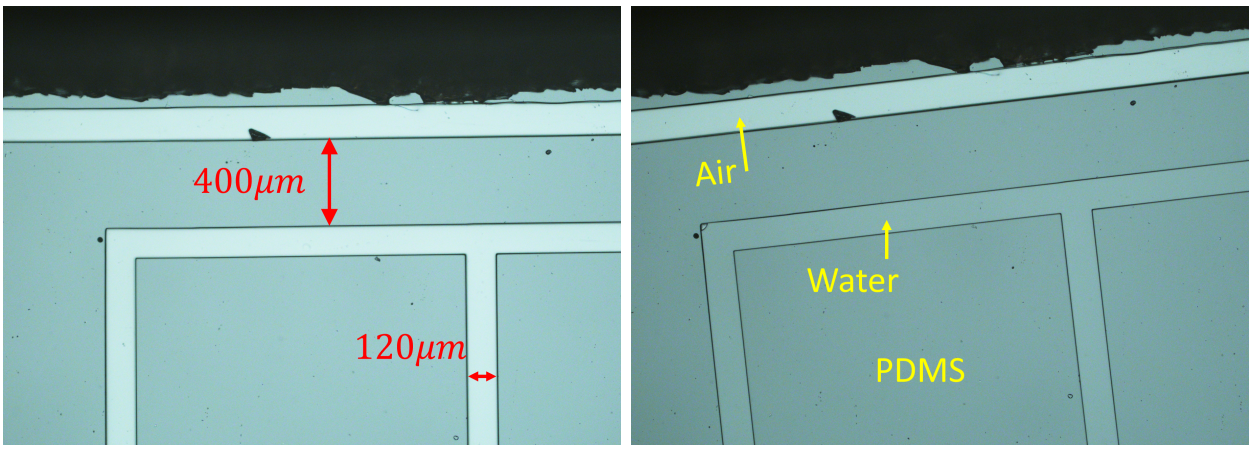

Figure 3.11: Microscope image of device before (left) and after (right) injecting water into it.

3.5 Integrating Multiple Interposers on a Single Motherboard

Due to time constraints, we did not have an opportunity to explore options for integrating multiple interposers on a single motherboard. This idea was sparked by a desire to have multiple quantum-enhanced bio-sensor on a single chip, which will not be relevant to our research for several years.

4 Future Work

4.1 Achieve repeatable alignment.

Our future fabrication of quantum-enhanced bio-sensor will rely heavily on our ability to precisely align our microfluidic channels to the waveguides on our photonic chips.

Aligning microfluidic channels to the racetrack resonators proved difficult for the following three reasons:

- The alignment tolerence is of the order of $\sim 100\mu m$.
- PDMS is a transparent material, so the channels may not be easily seen with the naked eye.
- The bond must be formed within a short time frame, as the surface of the PDMS only remains active for around 2 minutes after the oxygen plasma treatment.

Therefore, it is paramount that we either develop a reliable methodology for performing this alignment or devise an alignment-agnostic channel design.

In pursuit of the first option, we have designed an alignment jig, shown in Fig. 4.1 that is compatible with the PE-50. This jig should allow us to align our microfluidic channels to the corresponding waveguides under a microscope and lock everything into place before the plasma treatment.

Alternatively, we are considering simply etching the channels into oxide cladding of the photonic chip and using the interposer to connect to larger vias in the cladding, which would significantly reduce alignment constraints.

4.2 Optimize design of chips and channels.

In addition to refining our alignment techniques, we also plan to explore alignment agnostic designs. We have found examples of such designs by other research groups, which rely primarily

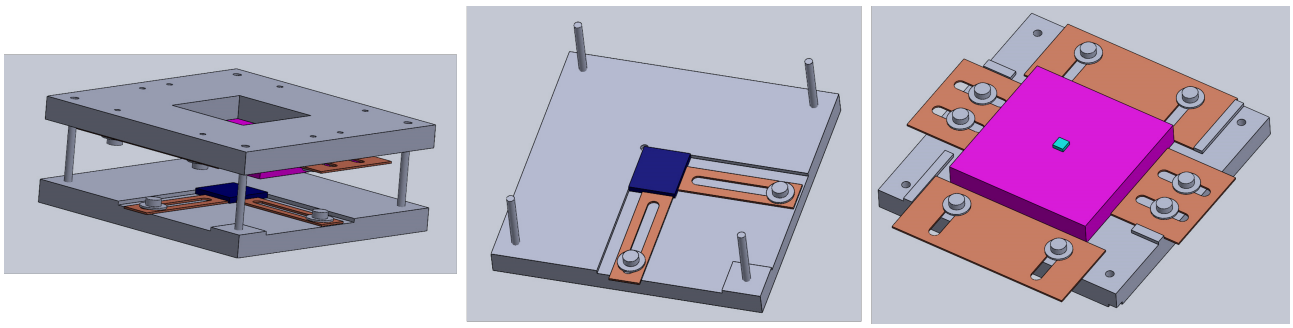

Figure 4.1: CAD design of the microfluidic channel of the real device.

on orienting their microfluidic channels perpendicular to the optical waveguides. See Fig. 4.2.

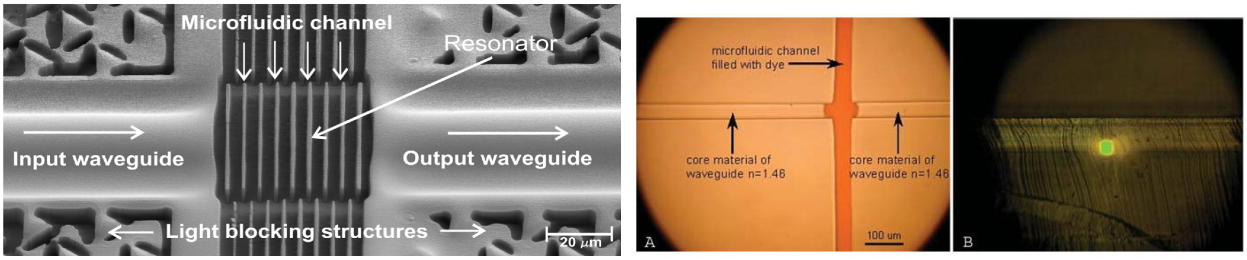

Figure 4.2: Microfluidic channel perpendicular to waveguide from [30](left) and [31](right).

Another important design consideration is optimizing the overlap between the optical mode and fluid within the microfluidic channels to maximize the interaction between the optical fiels and the sample. Two usual approaches include choosing TM mode[32, 33] and fabricating slot-waveguides[34, 35, 36]. We can use FDTD softwares such as Ansys Lumerical or COMSOL Multiphysics® to calculate numerically.

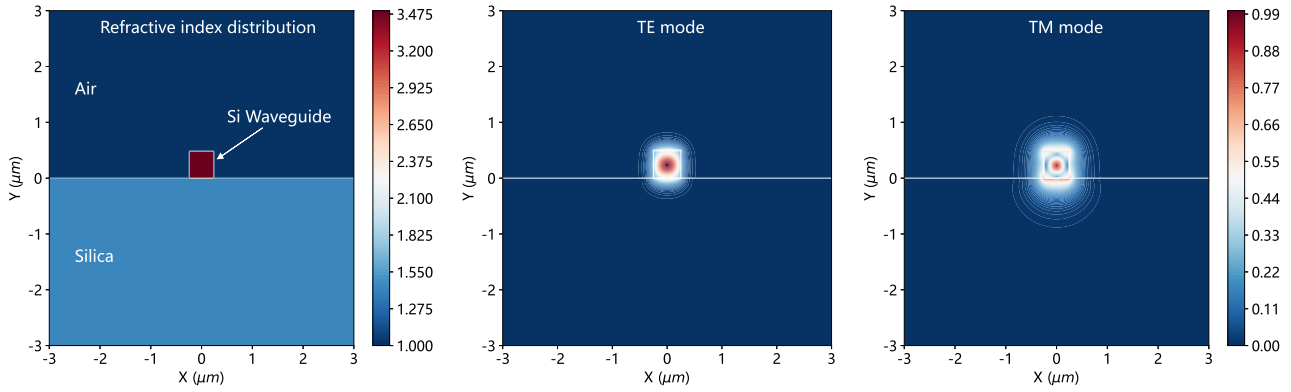

Figure 4.3: Design of Si waveguide(left) and TE(middle)/TM(right) mode at $1.55\mu m$.

In Fig. 4.3 we present a simple design of a single silicon waveguide on silica, with an air cladding. It is easy to see that TE mode is mostly confined within the Si waveguide while the TM mode extends beyond the waveguide. Therefore, using a TM-mode waveguide may prove useful in the future operation of our bio-sensors.

In Fig. 4.4 we present a design for a silicon slot waveguide on silica with air cladding. Because the electric field changes drastically at high index-contrast interfaces, this structure can enhance and confine light in the low index region, i.e, the gap between two Si waveguides[34]. If the sample flows in between the two slots, the interaction with optical field may be largely enhanced.

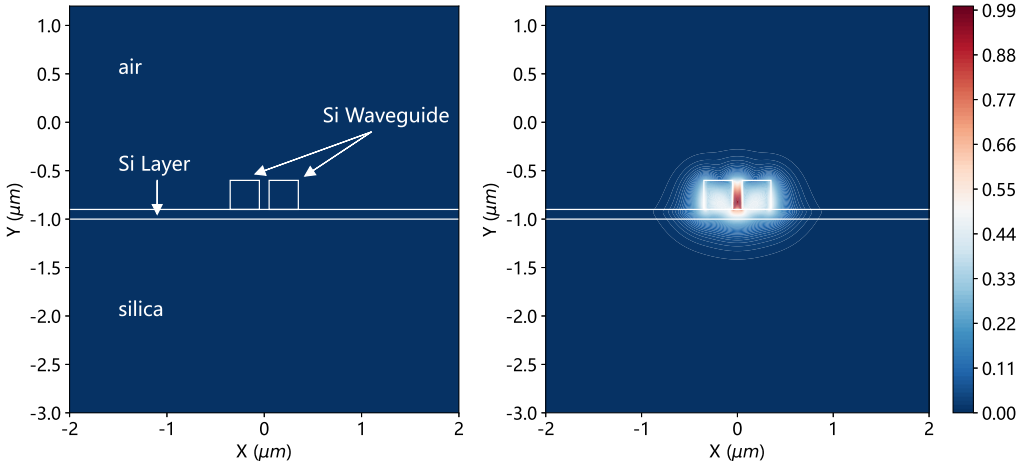

Figure 4.4: Design of Si slot waveguides and electric field distribution.

4.3 Investigate Sensing Applications.

While the ultimate goal of our quantum-enhanced sensor is to perform single molecule detection, we have devised a methodology to perform less stringent measurements, such as detecting gold nano-particles in a solution. Our measurement scheme takes advantage of the enhancement provided by an optical ring resonator by flowing a solution across the straight section of a racetrack resonator, as shown in Fig. 4.5.

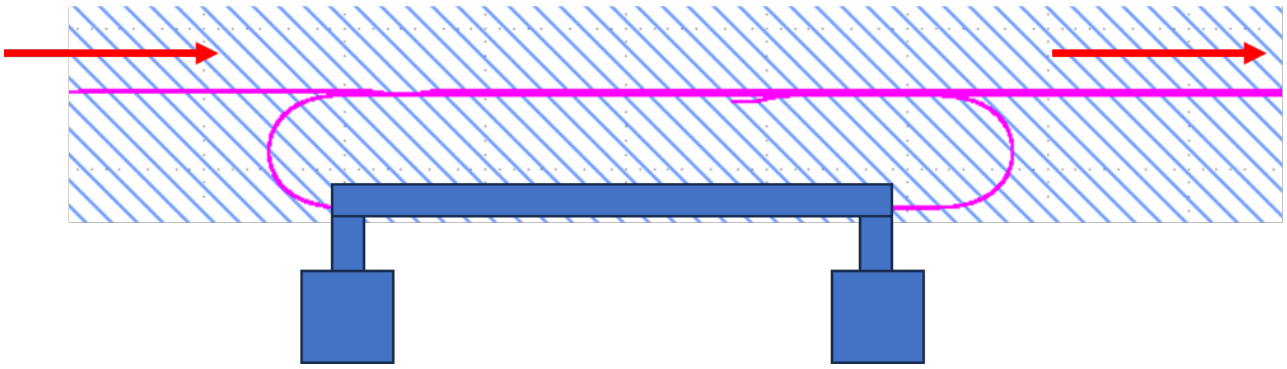

Figure 4.5: Resonator-Enhanced Nano-Particle Detection Scheme.

We would then park a laser at the steepest part of the resonator's transmission spectrum, as indicated by the purple line in 4.6, and measure changes in transmission caused by changes in effective refractive index induced by the presence of gold nano-particles. The change in power may be understood using the following equation:

$$P_t(\Delta n) = \left(1 - \frac{3C}{4}\right) P_i - \frac{3\sqrt{3}CQP_i}{4}\frac{\Delta n}{n} \tag{1}$$

where n is the refractive index, Δn is the change in refractive index induced by the nano-particles, P_i is the input power to the resonator, C is the contrast of resonance set by the coupling, and Q is the resonator's quality factor.

We can also estimate the smallest measurable change in refractive index in a shot-noise limited device to be:

$$\frac{\Delta n}{n} = \frac{4}{3CQ}\sqrt{\frac{\hbar\omega\left(1-\frac{3C}{4}\right)}{3T_{int}P_i}} = \frac{4}{3CQ}\sqrt{\frac{\left(1-\frac{3C}{4}\right)}{3N}} \tag{2}$$

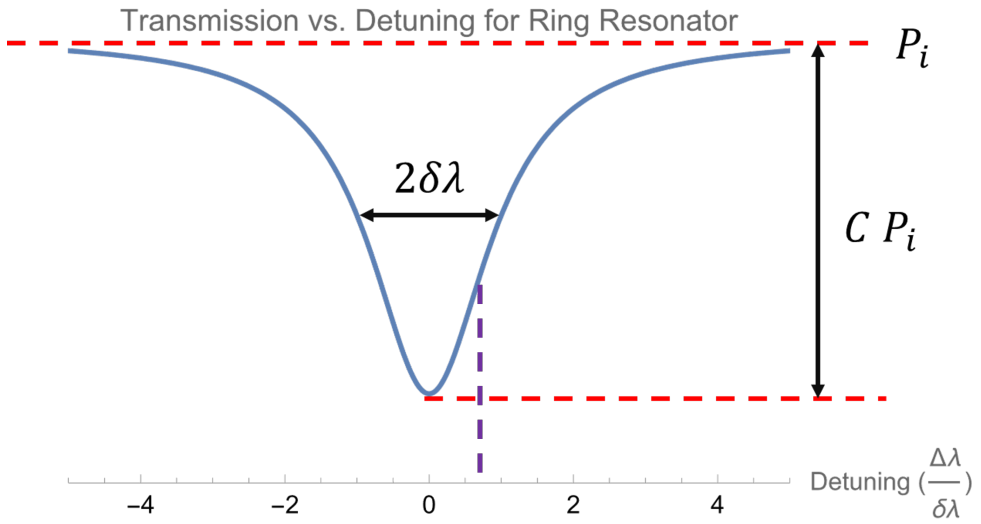

Figure 4.6: Transmission Spectrum of Ring Resonator.

where T_{int} is the integration time of the measurement and N is the number of incident photons that arrive at the resonator's input in the time T_int. We plan to test this measurement scheme in the coming months as an initial test piece for our microfluidic structures.

5 Budget

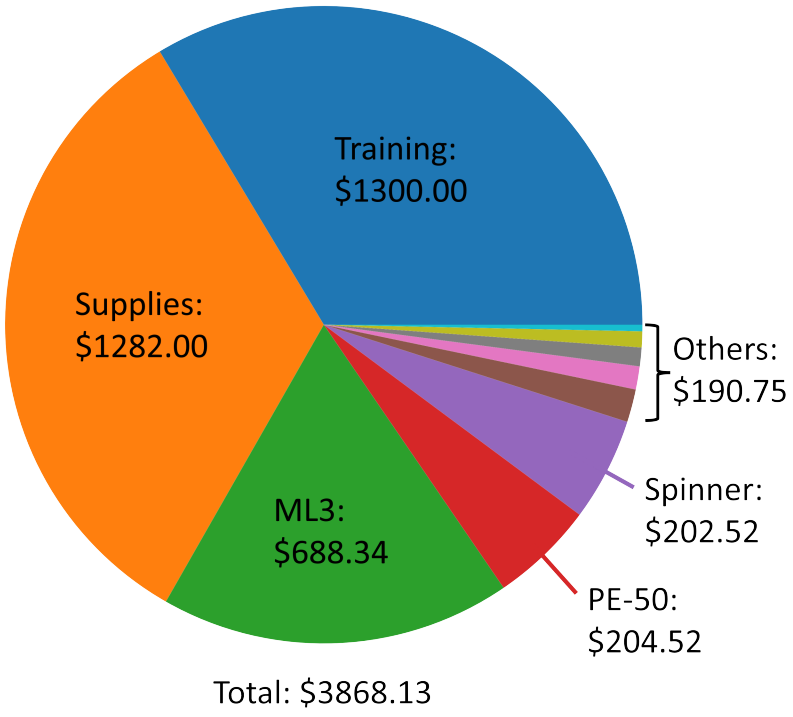

Figure 5.1: Budget Breakdown

6 Acknowledgement

This work is supported by Stanford Nanofabrication Facility (SNF) and Stanford Nano Shared Facilities (SNSF).

We would like to thank our mentors, Swaroop Kommera, J Provine, and Michelle Rincon, for their guidance and help during our weekly meetings.

We would like to thank Prof. Amir Safavi-Naeini, Taewon Park, Devin Dean, and Luke Qi in our research group. They helped us finish our proposal. Without them, the whole project wouldn't have been possible.

We also want to thank Michael Robles and Dave Huber whose experiences with microfluidics proved indispensable.

We would like to thank Rachel Gruenke for her guidance in the early stages of this project, as well as Sergio Cordero and Linus Woodard for teaching us how to use the DISCO wafer saw.

References

[1] Clifford R Pollock and Michal Lipson. *Integrated photonics*, volume 20. Springer, 2003. 1.1

[2] Emanuele Pelucchi, Giorgos Fagas, Igor Aharonovich, Dirk Englund, Eden Figueroa, Qihuang Gong, Hübel Hannes, Jin Liu, Chao-Yang Lu, Nobuyuki Matsuda, et al. The potential and global outlook of integrated photonics for quantum technologies. *Nature Reviews Physics*, 4(3):194–208, 2022. 1.1

[3] Hongtao Lin, Zhengqian Luo, Tian Gu, Lionel C Kimerling, Kazumi Wada, Anu Agarwal, and Juejun Hu. Mid-infrared integrated photonics on silicon: a perspective. *Nanophotonics*, 7(2):393–420, 2017. 1.1

[4] Bahram Jalali and Sasan Fathpour. Silicon photonics. *Journal of lightwave technology*, 24(12):4600–4615, 2006. 1.1

[5] David Thomson, Aaron Zilkie, John E Bowers, Tin Komljenovic, Graham T Reed, Laurent Vivien, Delphine Marris-Morini, Eric Cassan, Léopold Virot, Jean-Marc Fédéli, et al. Roadmap on silicon photonics. *Journal of Optics*, 18(7):073003, 2016. 1.1

[6] Shawn Yohanes Siew, Bo Li, Feng Gao, Hai Yang Zheng, Wenle Zhang, Pengfei Guo, Shawn Wu Xie, Apu Song, Bin Dong, Lian Wee Luo, et al. Review of silicon photonics technology and platform development. *Journal of Lightwave Technology*, 39(13):4374–4389, 2021. 1.1

[7] Wim Bogaerts, Dirk Taillaert, Bert Luyssaert, Pieter Dumon, Joris Van Campenhout, Peter Bienstman, Dries Van Thourhout, Roel Baets, Vincent Wiaux, and Stephan Beckx. Basic structures for photonic integrated circuits in silicon-on-insulator. *Optics Express*, 12(8):1583–1591, 2004. 1.1

[8] Bowei Dong, Xin Guo, Chong Pei Ho, Bo Li, Hong Wang, Chengkuo Lee, Xianshu Luo, and Guo-Qiang Lo. Silicon-on-insulator waveguide devices for broadband mid-infrared photonics. *IEEE Photonics Journal*, 9(3):1–10, 2017. 1.1

[9] Christof P Dietrich, Andrea Fiore, Mark G Thompson, Martin Kamp, and Sven Höfling. Gaas integrated quantum photonics: Towards compact and multi-functional quantum photonic integrated circuits. *Laser & Photonics Reviews*, 10(6):870–894, 2016. 1.1

[10] Jianwei Wang, Alberto Santamato, Pisu Jiang, Damien Bonneau, Erman Engin, Joshua W Silverstone, Matthias Lermer, Johannes Beetz, Martin Kamp, Sven Höfling, et al. Gallium arsenide (gaas) quantum photonic waveguide circuits. *Optics Communications*, 327:49–55, 2014. 1.1

[11] Meint Smit, Kevin Williams, and Jos Van Der Tol. Past, present, and future of inp-based photonic integration. *Apl Photonics*, 4(5), 2019. 1.1

[12] Shamsul Arafin and Larry A Coldren. Advanced inp photonic integrated circuits for communication and sensing. *IEEE Journal of Selected Topics in Quantum Electronics*, 24(1):1–12, 2017. 1.1

[13] Yifan Qi and Yang Li. Integrated lithium niobate photonics. *Nanophotonics*, 9(6):1287–1320, 2020. 1.1

[14] Andreas Boes, Lin Chang, Carsten Langrock, Mengjie Yu, Mian Zhang, Qiang Lin, Marko Lončar, Martin Fejer, John Bowers, and Arnan Mitchell. Lithium niobate photonics: Unlocking the electromagnetic spectrum. *Science*, 379(6627):eabj4396, 2023. 1.1

[15] Guanyu Chen, Nanxi Li, Jun Da Ng, Hong-Lin Lin, Yanyan Zhou, Yuan Hsing Fu, Lennon Yao Ting Lee, Yu Yu, Ai-Qun Liu, and Aaron J Danner. Advances in lithium niobate photonics: development status and perspectives. *Advanced Photonics*, 4(3):034003–034003, 2022. 1.1

[16] Juanjuan Lu, Ayed Al Sayem, Zheng Gong, Joshua B Surya, Chang-Ling Zou, and Hong X Tang. Ultralow-threshold thin-film lithium niobate optical parametric oscillator. *Optica*, 8(4):539–544, 2021. 1.1

[17] Cheng Wang, Mian Zhang, Mengjie Yu, Rongrong Zhu, Han Hu, and Marko Loncar. Monolithic lithium niobate photonic circuits for kerr frequency comb generation and modulation. *Nature communications*, 10(1):978, 2019. 1.1

[18] Mian Zhang, Brandon Buscaino, Cheng Wang, Amirhassan Shams-Ansari, Christian Reimer, Rongrong Zhu, Joseph M Kahn, and Marko Lončar. Broadband electro-optic frequency comb generation in a lithium niobate microring resonator. *Nature*, 568(7752):373–377, 2019. 1.1

[19] Cheng Wang, Mian Zhang, Xi Chen, Maxime Bertrand, Amirhassan Shams-Ansari, Sethumadhavan Chandrasekhar, Peter Winzer, and Marko Lončar. Integrated lithium niobate electro-optic modulators operating at cmos-compatible voltages. *Nature*, 562(7725):101–104, 2018. 1.1

[20] Wentao Jiang, Christopher J Sarabalis, Yanni D Dahmani, Rishi N Patel, Felix M Mayor, Timothy P McKenna, Raphaël Van Laer, and Amir H Safavi-Naeini. Efficient bidirectional piezo-optomechanical transduction between microwave and optical frequency. *Nature communications*, 11(1):1166, 2020. 1.1

[21] Hubert S Stokowski, Timothy P McKenna, Taewon Park, Alexander Y Hwang, Devin J Dean, Oguz Tolga Celik, Vahid Ansari, Martin M Fejer, and Amir H Safavi-Naeini. Integrated quantum optical phase sensor in thin film lithium niobate. *Nature Communications*, 14(1):3355, 2023. 1.1

[22] Rajveer Nehra, Ryoto Sekine, Luis Ledezma, Qiushi Guo, Robert M Gray, Arkadev Roy, and Alireza Marandi. Few-cycle vacuum squeezing in nanophotonics. *Science*, 377(6612):1333–1337, 2022. 1.1

[23] Taewon Park, Hubert Stokowski, Vahid Ansari, Samuel Gyger, Kevin KS Multani, Oguz Tolga Celik, Alexander Y Hwang, Devin J Dean, Felix Mayor, Timothy P McKenna, et al. Single-mode squeezed-light generation and tomography with an integrated optical parametric oscillator. *Science Advances*, 10(11):eadl1814, 2024. 1.1, 1.1, 2.3.3.1

[24] Lisa Barsotti, Jan Harms, and Roman Schnabel. Squeezed vacuum states of light for gravitational wave detectors. *Reports on Progress in Physics*, 82(1):016905, 2018. 1.1

[25] Benjamin J Lawrie, Paul D Lett, Alberto M Marino, and Raphael C Pooser. Quantum sensing with squeezed light. *Acs Photonics*, 6(6):1307–1318, 2019. 1.1

[26] Jacob B Nielsen, Robert L Hanson, Haifa M Almughamsi, Chao Pang, Taylor R Fish, and Adam T Woolley. Microfluidics: innovations in materials and their fabrication and functionalization. *Analytical chemistry*, 92(1):150–168, 2019. 1.1

[27] A del Campo and C Greiner. Su-8: A photoresist for high-aspect-ratio and 3d submicron lithography. *Journal of Micromechanics and Microengineering*, 17(6), May 2007. 2.3.1

[28] Hubert Lorenz, M. Despont, N. Fahrni, Nemtanu Bianca, P. Renaud, and Peter Vettiger. A low cost negative resist for mems. *Journal of Micromechanics and Microengineering - J MICROMECHANIC MICROENGINEER*, 7:121–124, 09 1997. 2.3.1

[29] Alexandra Borók, Kristóf Laboda, and Attila Bonyár. Pdms bonding technologies for microfluidic applications: A review. *Biosensors*, 11(8):292, Aug 2021. 2.3.3.1

[30] PS Nunes, Niels Asger Mortensen, Jörg Peter Kutter, and Klaus Bo Mogensen. Photonic crystal resonator integrated in a microfluidic system. *Optics letters*, 33(14):1623–1625, 2008. 4.2

[31] V Lien, H Lin, J Chuang, MJ Sailor, and YH Lo. Engineering in medicine and biology society, 2004. embc 2004. In *Conference Proceedings. 26th Annual International Conference of the 1*, 2004. 4.2

[32] Samantha M Grist, Shon A Schmidt, Jonas Flueckiger, Valentina Donzella, Wei Shi, Sahba Talebi Fard, James T Kirk, Daniel M Ratner, Karen C Cheung, and Lukas Chrostowski. Silicon photonic micro-disk resonators for label-free biosensing. *Optics express*, 21(7):7994–8006, 2013. 4.2

[33] Lucía Castelló-Pedrero, María I Gómez-Gómez, Jaime García-Rupérez, Amadeu Griol, and Alejandro Martínez. Performance improvement of a silicon nitride ring resonator biosensor operated in the tm mode at 1310 nm. *Biomedical Optics Express*, 12(11):7244–7260, 2021. 4.2

[34] Vilson R Almeida, Qianfan Xu, Carlos A Barrios, and Michal Lipson. Guiding and confining light in void nanostructure. *Optics letters*, 29(11):1209–1211, 2004. 4.2, 4.2

[35] Carlos A Barrios, Maria Jose Banuls, Victoria Gonzalez-Pedro, Kristinn B Gylfason, Benito Sanchez, Amadeu Griol, Angel Maquieira, Hans Sohlström, Miquel Holgado, and Rafael Casquel. Label-free optical biosensing with slot-waveguides. *Optics letters*, 33(7):708–710, 2008. 4.2

[36] Tom Claes, Jordi Girones Molera, Katrien De Vos, Etienne Schacht, Roel Baets, and Peter Bienstman. Label-free biosensing with a slot-waveguide-based ring resonator in silicon on insulator. *IEEE Photonics journal*, 1(3):197–204, 2009. 4.2